IEEE Access
Multidisciplinary | Rapid Review | Open Access Journal

Received July 13, 2020, accepted July 24, 2020, date of publication July 29, 2020, date of current version August 20, 2020.

Digital Object Identifier 10.1109/ACCESS.2020.3012694

Coupled Dynamic Modeling and Analysis of the Single Gimbal Control Moment Gyroscope Driven by Ultrasonic Motor

SONG PAN[1], (Member, IEEE), FAN ZHANG XU[1], LEI CHEN[1], WEIQING HUANG[2], AND JINTAO WU[3]

[1]State Key Laboratory of Mechanics and Control of Mechanical Structures, Nanjing University of Aeronautics and Astronautics, Nanjing 210016, China
[2]School of Mechanical and Electric Engineering, Guangzhou University, Guangzhou 510006, China
[3]Beijing Institute of Control Engineering, Beijing 100000, China

Corresponding authors: Song Pan (pansong@nuaa.edu.cn) and Fan Zhang Xu (471312538@qq.com)

This work was supported in part by the National Natural Science Foundation of China under Grant 51575260, and in part by the Beijing Key Laboratory of Long-Life Technology of Precise Rotation and Transmission Mechanisms under Grant BZ0388201804.

ABSTRACT A control moment gyroscope (CMG) is a key actuator for spacecraft's attitude and stability control. But there exist micro-vibrations from high-speed flywheel, which will affect the performance of the spacecraft greatly. Due to the unbalanced mass and the supporting structure, the high-speed rotating flywheel could generate disturbance torque, which will be passed to the gimbal to deteriorate the gimbal servo system. At the same time, the rotation of the gimbal will increase the disturbance torque for gyroscopic effect. According · to the bearing theory, the stiffness of the bearing is affected by the load that applied on it, which results the influence on the flywheel vibration and the generated disturbance torque. This means that there is a coupling effect in the CMG. In this article, we focused on this coupling relationship between the flywheel vibration and the gimbal rotation in a single gimbal control moment gyroscope (SGCMG) system. Firstly, a vibration model of the flywheel with variable stiffness supporting is established. And the rotation model of the gimbal is also developed. The flywheel model and the gimbal model are coupled with each other through the variable stiffness supporting and gyroscope effect. Based on the numerical simulations the interactions among the bearing stiffness, the flywheel vibration and the gimbal rotation are analyzed. Finally, experiments are carried out on the prototype. The experimental results have verified the theoretical analysis and the simulations, and which would support the design of high-performance control system.

INDEX TERMS Control moment gyroscope, ultrasonic motor, coupled model, dynamic stiffness.

I. INTRODUCTION

As actuator, CMG has been effectively used in space system [1], [2], single-wheel robotic system [3] and underwater robotic system [4] for its torque characteristics. SGCMG is a kind of CMG, which is widely used as a key internal momentum exchange device for its feature of torque amplification [5]–[7]. A SGCMG mainly includes high-speed flywheel system and low-speed gimbal system. Traditionally, both the systems are driven by electromagnetic motor [8], [9]. It is very meaningful to find new actuator to reduce the weight of the SGCMG. The USM has been developed as a new concept of motor since the 1980's [10]. It utilizes the vibration of the elastic body (stator) in the ultrasonic frequency range, which excited by a group of piezoelectric materials based on the reverse piezoelectric effect. The mechanical movement and torque are obtained by means of the frictional contact force between the stator and the rotor. In 2013, the USM has been successfully used in lunar rover Yutu of China [11]. Due to the good temperature adaptability, two USMs were used for a space robotic arm [12]. These applications show the unique advantage of the USMs in the aerospace engineering. In this article, a SGCMG directly driven by an USM is presented.

For high-precision observation application, the satellites should have high precision pointing performance, unfortunately which will be affected by the micro-vibration on the spacecraft [13]–[16]. When the SGCMG act as the momentum exchange actuator of the spacecraft altitude control,

The associate editor coordinating the review of this manuscript and approving it for publication was Zhong Wu.

it's micro-vibration for the flywheel's dynamic unbalance is the most prominent sources of the disturbance [17], [18]. It has attracted the attentions of researchers to address the micro-vibration problem in the CMG [19]–[21]. The mass imbalance of the flywheel is typically considered as the main source of the disturbance, more importantly, it would stir up more complex behavior. The amplitudes of the disturbing force and torques caused by the mass imbalance are proportional to the square of the angular speed [22]. The vibration from the flywheel affects the rotation of the gimbal through the supporting bearing and mechanical structure. For the high-speed flywheel system, the influence of the bearing is considered as an important factor from the point of view of the dynamic analysis. In a high-speed rotating system, the bearing's stiffness is time-varying, and it is affected by the load that applied on the bearing [23], [24]. Besides, the existence of the imbalance can lead to the simultaneous backward and forward precessions of the rotor [25].

In a SGCMG, what should not be overlooked is the gyroscope effect. The rotation of the gimbal would affect the stiffness of the bearing, and then result in complex coupled motion between the flywheel and the gimbal, which could deteriorate the running of the system [26]–[28]. Considering the static and dynamic imbalances and installation errors of the flywheel, reference [29] analyzed the disturbance characteristic of CMG. A gimbal disturbance observer is constructed to estimate the dynamic imbalance of the CMG's rotor in [30], and a third-order dynamic model is presented to describe the gimbal servo system. An output torque model of SGCMG is conducted in [31], which considers the bearing supports and the installation errors and mainly focus on the static running station of the gimbal.

The gimbal systems of the SGCMG aforementioned are driven by electromagnetic motor. For the gimbal directly driven by USM, the friction driving mechanism makes it different [32]. In this research, we focus on a SGCMG directly driven by an USM and construct a coupled model of the SGCMG. In this model the time-varying stiffness supporting of the flywheel is considered. Considering the radial load, the stiffness model of the bearing is established. Since the rotating movement of the gimbal is driven through the friction between the stator and the rotor of the USM, the LuGre friction model is introduced to describe the rotation dynamics of the gimbal. The numerical simulation and experiments are carried out to verify the presented coupled model of the SGCMG.

The remainder of this article proceeds as follows: Section II describes the mechanical structure of the SGCMG driven by the USM. Section III provides the coupled model of the SGCMG. Section IV presents and discusses the numerical and experimental results of the coupled model and the normal model. Section V compares experimental results with the numerical simulations. Finally, Section VI summarizes the paper and states the conclusions.

II. STRUCTURE OF THE SGCMG

A typical structure of a SGCMG consists of a flywheel, a gimbal, a rotor motor, and a gimbal motor as shown in Fig. 1. The flywheel is supported by the gimbal and is driven by the rotor motor with the angular velocity of $\boldsymbol{\Omega}$. Assuming the moment of inertia of the flywheel and the rotor motor is J, the angular momentum of $\mathbf{L}$ could be described as $\mathbf{L} = J \cdot \boldsymbol{\Omega}$. The gimbal is driven by the gimbal motor with the speed of $\boldsymbol{\omega}$. The direction of $\mathbf{L}$ is changed with the rotating of the gimbal, at the same time a torque T is generated due to the gyroscopic effect. The induced torque can be described as

$$T = \boldsymbol{\omega} \times \mathbf{L} = \boldsymbol{\omega} \times J \cdot \boldsymbol{\omega}. \tag{1}$$

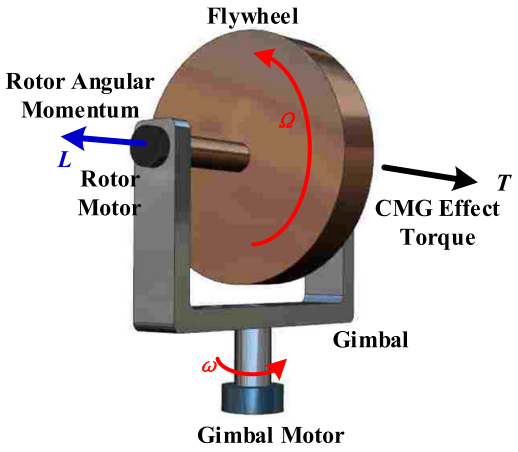

FIGURE 1. Traditional structure and working principle of the SGCMG.

The T is the driver source for attitude control of a satellite or other spacecrafts. Generally, the $\boldsymbol{\Omega}$ is kept working at a constant velocity, so the T was determined by the gimbal velocity of $\boldsymbol{\omega}$.

Considering the advantage of high accuracy and fast response of a USM, a SGCMG directly driven by a hollow USM was designed in our project. The structure of the SGCMG driven by the USM is shown in Fig. 2. The flywheel was directly driven by a brushless direct-current (BLDC) motor. The rotor of the BLDC and the flywheel were integrated designed for compactness. The stator of the BLDC was fixed on the gimbal. The flywheel, the BLDC and their supporting shaft are high speed rotating parts, which were supported by the gimbal through two high-speed bearings. The gimbal was installed on the base through two low-speed bearings. The gimbal was connected directly with the rotor of the USM through a fit surface and a flat key. The stator of the USM was fixed on the base. A high precision encoder was fixed on the base and was used to measure the rotation of the gimbal. The assembled SGCMG was installed on the spacecraft through the base. With the high-speed rotating of the flywheel, the vibration generated by the flywheel could couple with the rotating of the gimble, which is the major research of this article.

The structure of the flywheel has very important impact on the vibrating suppression. The BLDC motor has the

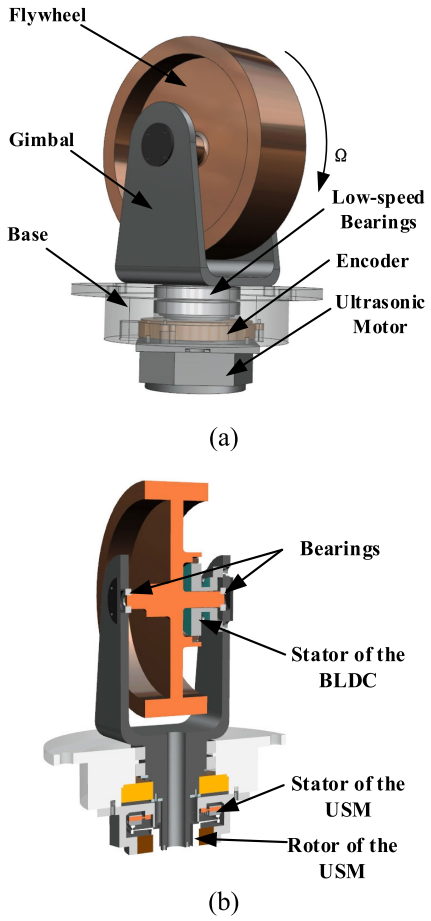

FIGURE 2. (a) The structure of the SGCMG driven by ultrasonic motor, (b) The cross section of the SGCMG.

advantages of small size, long lifespan and high efficiency, so a BLDC-coupled flywheel for this SGCMG was designed. The structure of the flywheel is shown in Fig. 3. The BLDC-flywheel integrated design makes it to be a compacted structure. The flywheel is made of phosphor bronze and seven pairs of magnetic poles (Neodymium Magnet) are stuck in the slots of the plate, which is shown in Fig. 3(a). An auxiliary installment made of duralumin was designed to positioning the magnets at the radius direction. To reduce the influence of the magnetic ring, a balance mass was designed at the other side of the flywheel as shown in Fig. 3(b).

III. MODEING OF THE SYSTEM

The SGCMG consists of two main dynamic components: the flywheel and the gimbal. The flywheel and the gimbal are both modelled as rigid rotors as their spinning speed are far below the first critical speed point. Benefiting from the mature control strategies of the BLDC motor, the flywheel speed fluctuation error can be controlled below 0.1%. The speed of the flywheel is considered as constant. As supports, the internal bearing systems connect the flywheel with the gimbal, which introduces two sets of vibrating systems in the SGCMG: namely the flywheel-bearing system and

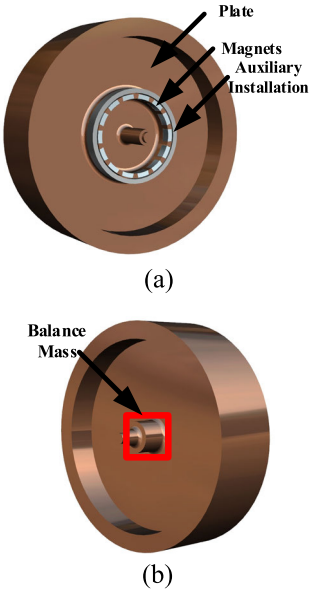

FIGURE 3. (a) The structure of the flywheel BLDC-coupled flywheel, (b) The design of balance mass.

gimbal-bearing system. For the gimbal-bearing system, the vibration is neglected because the gimbal usually running at low speed and the bearing's supporting stiffness is high enough. Therefore, the main research and analysis of the SGCMG are focused on the dynamic vibration of the flywheel-bearing system, the rotation of the gimbal and their coupling.

A. PREREQUISITES AND ASSUMPTIONS

The micro-dynamic system of the flywheel is a multi-degree-of-freedom (MDOF) system and its kinematics is complicated. For convenience, we should make some pre-requisites and assumptions and introduce the coordinate systems.

Prerequisites and assumptions:

- The flywheel has high stiffness, which is regarded as a rigid body.
- The static unbalance of the flywheel is ignored, that is only the dynamic unbalance is considered.
- The vibration satisfies the small deformation assumption.
- The translational degrees of freedom (DOF) are neglected, only the rotational DOF are introduced.
- The influence of the satellites is ignored.

The coordinate systems:

- $Oxyz$ is an inertial coordinate defined in the interface between the gimbal and its mounting surface.
- $Ox_sy_sz_s$ is an inertial coordinate fixed in the space.
- $Ox_wy_wz_w$ is an assistance coordinate describing the rocking vibration of the flywheel.
- $Ox_fy_fz_f$. is a rocking coordinate, which vibrates with the flywheel's rotating axis.

B. VIBRATION EQUATION

The flywheel is supported by two bearings. At high speeds the dynamic characteristics of the bearing would impact the rotation of the flywheel, which could bring serious gyroscopic effect and would introduce disturbance torque to the gimbal running. So, it is needed to model the working states and analyze how it impacts the gimbal system. The simplified mechanical model of the flywheel with supports is illustrated in Fig. 4. As shown in Fig. 4(a) the two bearings between the gimbal and shaft of the flywheel are modelled as spring and damper, and the flywheel are modelled as a rigid plate. The flywheel has dynamic unbalance due to manufacturing and assembly errors and heterogeneity of the material. The dynamic unbalance is modelled as shown in Figure 4(b), where m_{d} is the unbalanced mass and F_{d} is the force generated by the m_{d}.

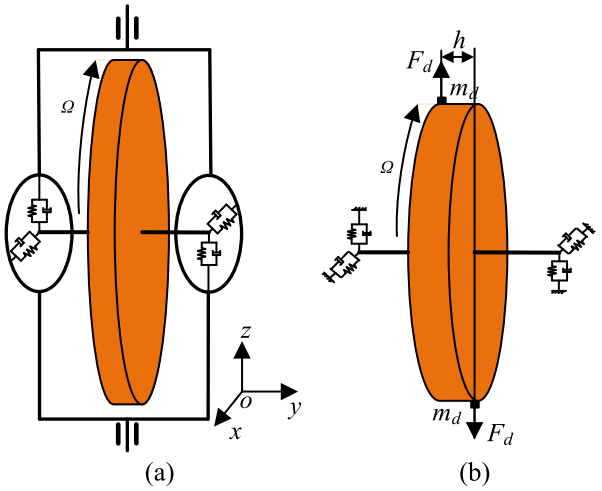

FIGURE 4. (a) Vibrating model of the flywheel, (b) Model considering the unbalanced mass.

The dynamic unbalance is an exciting force which would lead to vibration of the flywheel, then an imbalance torque is introduced. The imbalance torque T_{u} has relevant to the mechanical parameters and the velocity of the flywheel is shown in Eq. (2) [22].

$$T_u = U_d \mathbf{\Omega}^2 = m_d r h \mathbf{\Omega}^2, \tag{2}$$

where U_d is the dynamic unbalance weight of the flywheel, r is the equivalent radius of rotation of the m_{d} and h is the equivalent distance of the imbalance mass.

Considering the stiffness of bearing system, a 6- DOF vibration model is introduced [22]. In this model, both the translation and the rotation of the bearing were considered. Theoretically, the translation will not introduce the gyroscopic effect and will have few impacts on the gimbal system of the SGCMG, so here it is omitted. In fact, the vibration around x axis and around y axis would coupling with the rotation of z axis, which will generate the gyroscopic effect and is the vibrating source of gimbal axis. Considering the stiffness of the bearing, the flywheel has a rotation at the direction of radius. The generalized angular motion of the flywheel is described by the Euler Angle in Fig. 5.

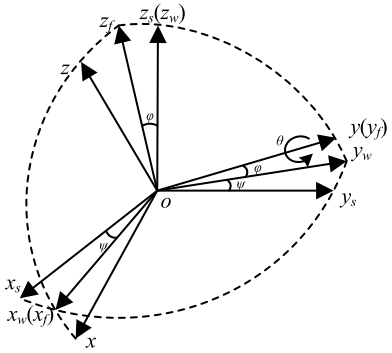

FIGURE 5. The generalized angular motion of the flywheel.

In Fig. 5 the original coordinate $Ox_sy_sz_s$ is fixed on the gimbal, which is as same as the coordinate in Fig. 4(a). The first rotation ψ is about the Oz_s axis, resulting in coincidence with $Ox_wy_wz_w$. The second rotation φ is about the Ox_w axis, resulting in coincidence with $Ox_{\mathrm{f}}y_{\mathrm{f}}z_{\mathrm{f}}$. The flywheel's spinning θ is about Oy_{f} axis, resulting in coincidence with $Oxyz$. The flywheel spinning speed is expressed as $\Omega = \dot{\theta}$.

The velocity of the flywheel is usually kept at a constant value. The rotating angle φ and ψ are selected as the variable parameters of the generalized coordinate vector $\mathbf{q}$, and it can be expressed as

$$\mathbf{q} = \begin{bmatrix} \varphi & \psi \end{bmatrix}^T. \tag{3}$$

The vibration equation of the flywheel-bearing system is expressed as

$$\begin{bmatrix} I_r & 0 \\ 0 & I_r \end{bmatrix} \ddot{\mathbf{q}} + \left(\begin{bmatrix} c_\varphi & 0 \\ 0 & c_\psi \end{bmatrix} + \mathbf{G} \right) \dot{\mathbf{q}} + \begin{bmatrix} k_\varphi & 0 \\ 0 & k_\psi \end{bmatrix} \mathbf{q} = \mathbf{Q}, \tag{4}$$

where I_r is the radial moments of the inertia, c_φ and c_ψ are the damping, k_φ and k_ψ are the stiffness and $\mathbf{G}$ is the coupling matrix generated by the gyroscopic effect, which can be expressed as

$$\mathbf{G} = \Omega \begin{bmatrix} 0 & I_p \\ -I_p & 0 \end{bmatrix}, \tag{5}$$

where I_p is the polar moments of the inertia. The matrix $\mathbf{Q}$ is the generalized force of this system, which is generated by the dynamic unbalance. From the coordinates in Fig.5, according to the rotating angle φ and ψ the $\mathbf{Q}$ has the expressed of

$$\mathbf{Q} = T_u \begin{bmatrix} \cos(\Omega t) \\ \sin(\Omega t) \end{bmatrix}. \tag{6}$$

C. MODELING OF THE BEARING

The supporting bearings of the flywheel are single-row deep-grove ball bearing. For high-speed ball and roller bearings, the rolling element centrifugal forces and the gyroscopic moments become significant. The damping and stiffness coefficient are important factors in the vibration Eq. (4).

In this section, the bearing stiffness model under gyroscopic moment load is established. A simplified contact model using the Hertz theory [27], [33] is introduced. The section view of the bearing, the contact between the ball and the inner raceway and the contact between the ball and the outer raceway are shown in Fig. 6(a). The equivalent analytical model of the bearing is shown in Fig. 6(b).

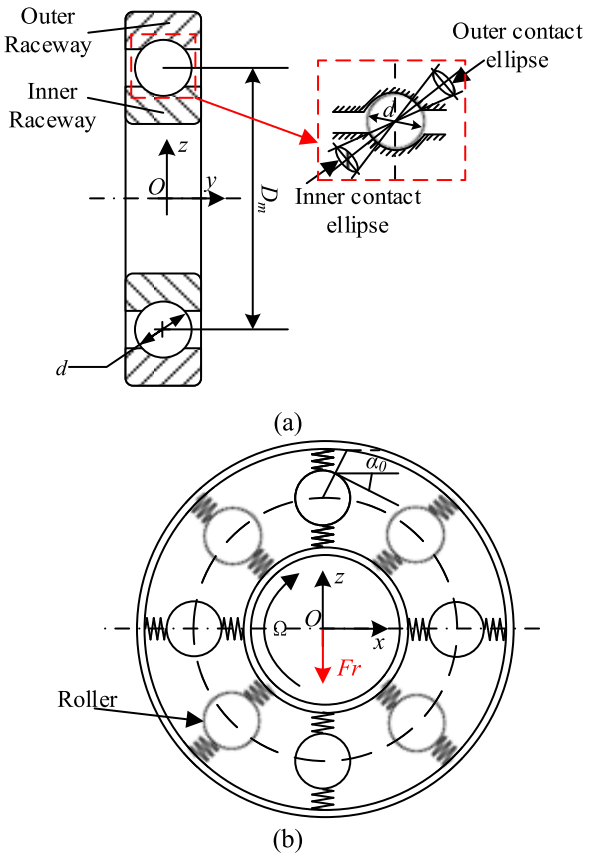

FIGURE 6. Analytical model of bearing: (a) The profile of the bearing, (b) The model of the bearing.

The stiffness of the rolling bearing is the ability to resist elastic deformation under the radial load. The stiffness of the deep groove ball bearing is defined as

$$k = \frac{\Delta F_r}{\Delta \delta}, \tag{7}$$

where ΔF_r is the radial force applied on the bearing and $\Delta\delta$ is the radial offset of the bearing center which is approximately equal to the deformation of the roller under the largest force. For the flywheel of the SGCMG, the radial force is generated by the gyroscopic effect. The torque of the flywheel is calculated by the Euler equation

$$\mathbf{T} = \dot{\mathbf{H}} + \boldsymbol{\omega} \times \mathbf{H} = \begin{bmatrix} I_r\ddot{\phi} \\ I_p\dot{\Omega} \\ I_r\ddot{\psi} \end{bmatrix} + \begin{bmatrix} \dot{\phi} \\ \Omega \\ \dot{\psi} + \omega \end{bmatrix} \times \begin{bmatrix} I_r\dot{\phi} \\ I_p\Omega \\ I_r\dot{\psi} \end{bmatrix}, \tag{8}$$

where ω is the velocity of the gimbal. Because the rotational velocity of the flywheel is constant, and ignore the high-order term, the generated torque is expressed as

$$\begin{bmatrix} T_x \\ T_y \\ T_z \end{bmatrix} = \begin{bmatrix} I_r\ddot{\phi} + \omega I_p\Omega + \dot{\psi}I_r\Omega \\ 0 \\ I_r\ddot{\psi} + \omega I_r\dot{\phi} - \dot{\phi}I_r\Omega \end{bmatrix}. \tag{9}$$

Since the amplitude of micro-vibration is very small, the output torque generated by the micro-vibration is much smaller than that generated by the rotation of the gimbal. According to the supporting, the radial load of the bearing could be calculated and expressed as

$$F_r = \frac{T_x + T_z}{l} = \frac{\omega I_p\Omega}{l}, \tag{10}$$

where l is the distance between the supporting bearings.

According to the point contact theory of Hertz [34], δ_i and δ_o are the contact deformation of the inner and outer raceway respectively and cab be expressed as

$$\delta_i = \left(\frac{4.5K_i^3(k_i)\sum\rho_i}{\pi^2E^2k_i^2E_i(k_i)}\right)^{\frac{1}{3}} Q_d^{\frac{2}{3}} \tag{11}$$

$$\delta_o = \left(\frac{4.5K_o^3(k_o)\sum\rho_o}{\pi^2E^2k_o^2E_o(k_o)}\right)^{\frac{1}{3}} Q_d^{\frac{2}{3}} \tag{12}$$

where K_i and K_o are the first class of completely elliptic integrals of inner and outer raceway contact ellipses, respectively, E_i and E_o are the second class of completely elliptic integrals of inner and outer raceway contact ellipses, respectively, k_i and k_o are the coefficient of the inner and outer raceway contact ellipses, respectively, and have the next expression

$$\begin{cases} 1/k_i^2 = 1 - e_i^2 \\ 1/k_o^2 = 1 - e_o^2, \end{cases} \tag{13}$$

where e_i *and* e_o are the eccentricity of the inner and outer raceway ellipse. E is the equivalent elastic modulus of the contact pair, which is expressed as

$$\frac{2}{E} = \frac{1 - \nu_r^2}{E_r} + \frac{1 - \nu_R^2}{E_R}, \tag{14}$$

where ν_r and ν_R are the Possion's ratio of the roller and the raceway, respectively, E_r and E_R are the elastic modulus of the roller and the raceway, respectively. $\Sigma\rho_i$ and $\Sigma\rho_o$ are the sum of the principal curvatures at the contact point of the outer and inner raceway, respectively, and can be expressed as

$$\sum\rho_i = \frac{1}{d}(4 + \frac{2\gamma}{1-\gamma} - \frac{1}{f_i}), \tag{15}$$

$$\sum\rho_o = \frac{1}{d}(4 - \frac{2\gamma}{1+\gamma} - \frac{1}{f_o}), \tag{16}$$

where d is the diameter of the roller which is shown in Fig. 6, f_i and f_o are the inner and outer raceway curvature radius coefficient which values range from 0.515 to 0.525 for the deep groove ball bearing [20], and γ is the bearing coefficient and has the next expression

$$\gamma = \frac{d\cos\alpha_0}{D_m}, \tag{17}$$

where D_m is the nominal diameter of the bearing which is shown in Fig. 6 and α_0 is the initial contact angle of the bearing.

In Eq. (11) and (12) Q_d is the largest contact stress of the roller in the bearing. For the deep groove ball bearing the contact stress is expressed as [34]

$$Q_d = \frac{4.37F_r}{Z}, \tag{18}$$

where Z is the number of the roller.

From Eq. (11), (12) and (18) we have

$$\delta_i = 2.0573\sqrt[3]{\frac{K_i^3(k_i)\sum\rho_i}{E^2k_i^2E_i(k_i)}(\frac{F_r}{Z})^2}, \tag{19}$$

$$\delta_i = 2.0573\sqrt[3]{\frac{K_o^3(k_o)\sum\rho_o}{E^2k_o^2E_o(k_o)}(\frac{F_r}{Z})^2}. \tag{20}$$

Let $A = 2.0573\sqrt[3]{\frac{K_i^3(k_i)\sum\rho_i}{E^2k_i^2E_i(k_i)Z^2}}$ and $B = 2.0573\sqrt[3]{\frac{K_o^3(k_o)\sum\rho_o}{E^2k_o^2E_o(k_o)Z^2}}$. According to the Hertz's theory, the total contact deformation of the bearing is expressed as

$$\delta = \delta_o + \delta_i = (A+B)F_r^{\frac{2}{3}}. \tag{21}$$

Substitute Eq. (10) and (21) into Eq. (7), the stiffness of the bearing is expressed as

$$k = \frac{3}{2}(A+B)^{-1}F_r^{\frac{1}{3}} = \frac{3}{2}(A+B)^{-1}\sqrt[3]{\frac{\omega I_p\Omega}{l}}. \tag{22}$$

The stiffness of the bearing is determined by the structure parameters and the load that applied on the bearing. The theoretical analysis of Hertz's point contact has relation with the structure parameters. The contact area between the roller and the raceway is an ellipse. The roller diameter d, the nominal diameter of the bearing D_m, the initial contact angle α_0 and the raceway curvature radius coefficient $f_{i,o}$ are all have effect on the contact area. The contact deformation is affected by the coefficient of the contact ellipse $e_{i,o}$, the curvature radius $\Sigma\rho_{i,o}$, the roller number Z and the Load F_r. The load that applied on the bearing is generated by the rotation of the flywheel and the gimbal. This stiffness model of the bearing coupling of the vibration of the flywheel and the rotation of the gimbal.

D. VIBRATION OF THE FLYWHEEL

The flywheel is installed on the gimbal through the bearing. Considering the stiffness of the bearing, this high-speed rotation system is simplified as the rotation flywheel supported by the variable stiffness spring, which is shown in Fig. 4.

As the stiffness of the bearing is calculated and shown in Eq. (22). To obtain the vibration characteristic with variable stiffness of the flywheel, the vibration mode of the flywheel-bearing system is calculated. The bearing has the same stiffness in all directions, since the structure of the bearing is axial symmetry. The damping caused by the bearing is also ignored. According to Eq. (4), the simplified vibration equation is expressed as

$$\begin{bmatrix} I_r & 0 \\ 0 & I_r \end{bmatrix}\begin{bmatrix} \ddot{\phi} \\ \ddot{\psi} \end{bmatrix} + \Omega\begin{bmatrix} 0 & I_p \\ -I_p & 0 \end{bmatrix}\begin{bmatrix} \dot{\phi} \\ \dot{\psi} \end{bmatrix} + \begin{bmatrix} k_\phi & 0 \\ 0 & k_\psi \end{bmatrix}\begin{bmatrix} \phi \\ \psi \end{bmatrix} = T_u\begin{bmatrix} \cos(\Omega t) \\ \sin(\Omega t) \end{bmatrix}, \tag{23}$$

where the rotational stiffness k_Φ and could be expressed as

$$k_\phi = \frac{1}{2}kl^2. \tag{24}$$

The eigen frequency of the vibrating system are gotten that

$$\omega_{n1,2} = \frac{\Omega I_p}{2I_r} \pm \sqrt{(\frac{\Omega I_p}{2I_r})^2 + k_\phi}. \tag{25}$$

The circular frequency ω_{n1} and ω_{n2} is affected by the spinning speed of the flywheel. In fact, ω_{n1} and ω_{n2} describe the precession of the flywheel in two direction, the direction of the precession is related to the velocity of the flywheel and the gimbal. If the precession has the same direction with the flywheel, it called forward precession as shown in Fig. 7(a). If the precession has the different direction with the flywheel, it called backward precession as shown in Fig. 7(b). The red arrow in Fig.7 is the direction of the precession, and the black arrow is the direction of the rotation.

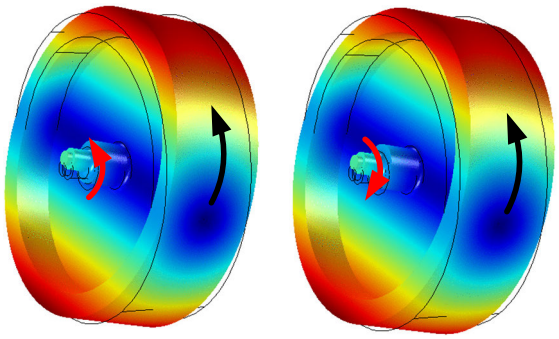

FIGURE 7. Vibration mode of the flywheel-bearing system: (a) Forward precession, (b) Backward precession.

E. MODELING OF THE GIMBAL

From Eq. (9), there is a coupling between the gimbal rotation and the flywheel rotation for gyroscopic effect. A gyroscopic torque (T_x in Eq. 9) would be induced, which has the same direction of the gimbal and would deteriorate the rotation of the gimbal greatly. In this section, the dynamic model of the gimbal considering the effect of the gyroscopic torque is researched. The gimbal is connected directly with the rotor of the USM and is driven through the friction between the rotor and the stator of the USM. The friction driving mechanism of the USM is shown in Fig. 8. On the stator a traveling wave is formed under the exciting of two group of piezoelectric ceramics (PZTs) pasted on the stator. The PZTs are driven

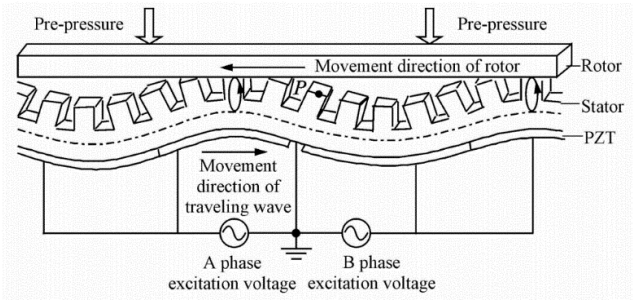

FIGURE 8. The friction driving mechanism of the USM.

by two alternating voltage with equal amplitude, same frequency and phase shift α in ultrasonic range. A more detailed description of the working process could be found in [10].

The LuGre model is introduced to describe the friction driving between the stator and the rotor of the USM [32]. Considering the gyroscopic torque, the dynamic equation of the rotor and the gimbal could be described as

$$(I_R + I_r + I_{gy})\dot{\omega} + C_R\omega = r_0(\sigma_0\xi + \sigma_1\dot{\xi}) - T_z, \quad (26)$$

where I_R is the inertia of the USM's rotor, I_{gy} is the inertia of the gimbal, C_R is the damping coefficient, r_0 is the mean radius of the rotor contact area, σ_0 is the spring-like coefficient, σ_1 is the micro-damping coefficient, T_z is the torque component in the z direction, which is shown in Eq. (9) and the variable ξ is the internal friction state. The friction state ξ characterized the friction interface between the rotor and the stator, and can be expressed as

$$\dot{\xi} = \omega_{st} - \omega - \sigma_0\frac{|\omega_{st} - \omega|}{g(\omega_{st} - \omega)}\xi, \quad (27)$$

$$g(\omega_{st} - \omega) = F_C + (F_S - F_C)e^{\frac{-(\omega_{st}-\omega)^2}{\omega_s^2}}, \quad (28)$$

where F_C is the Coulomb friction and F_S is the Stribeck friction, satisfying $F_C < F_S$. These two parameters are determined by the contact pressure between the stator and the rotor of the USM. ω_s is the Stribeck velocity. ω_{st} is the maximum tangential velocity of the traveling wave on the stator and can be expressed as

$$\omega_{st} = cV_0\frac{2\pi f}{\sqrt{(1 - \frac{f^2}{f_n^2}) + (2\zeta\frac{f}{f_n})^2}}\sin(\alpha), \quad (29)$$

where c is the mechanical coefficient, V_0 is the voltage of the driving signal, f is the frequency of the driven signal, f_n is the eigen frequency of the stator and ζ is the damping coefficient of the stator.

The LuGre friction model characterizes a series of known friction properties, such as Stribeck effect and stick-slip motion and produces an approximated hysteresis curve. As a result, the system's model becomes higher and complex. In this article, our goal is to establish a model that can characterize the major features of the USM, so a simpler friction dynamic model is welcome. According to [35], the friction dynamics is much faster than the rotor and the gimbal system. Therefore, it can be assumed that

$$\dot{\xi} = 0, \quad (30)$$

$$\xi = \frac{1}{\sigma_0}g(\omega_{st} - \omega)\mathrm{sgn}(\omega_{st} - \omega). \quad (31)$$

Then the dynamic equation is

$$(I_R + I_r + I_{gy})\dot{\omega} + C_R\omega = r_0 g(\omega_{st} - \omega)\mathrm{sgn}(\omega_{st} - \omega) - T_z. \quad (32)$$

There is nonlinear part in Eq. (28). For further simplification of the calculation, the Taylor's expansion is applied and the Eq. (32) could be simplified as

$$(I_R + I_r + I_{gy})\dot{\omega} + C_R\omega = r_0[F_S - (F_S - F_C)\frac{(\omega_{st} - \omega)^2}{\omega_s^2}]\mathrm{sgn}(\omega_{st} - \omega) - T_z. \quad (33)$$

F. COUPLING ANALYSIS

As can be seen from the above analysis that the SGCMG is a coupled system. The vibration of the flywheel and the rotation of the gimbal have interaction each other. On the one hand, the velocity of the gimbal affects the radial load that applied on the bearing as shown in Eq. (9). The stiffness of the bearing is changed by the radial load according to Eq. (22). Therefore, the vibration characteristic calculated by Eq. (23) is affected. On the other hand, the micro-vibration of the flywheel introduces the disturbance torque in the radial direction, which are passed to the gimbal according to the gyroscopic effect in Eq. (9). According to Eq. (33) the rotation speed of the gimbal is affected by the disturbance torque T_z. The coupling mechanism between the vibration of the flywheel and the rotation of the gimbal could be described in Fig. 9.

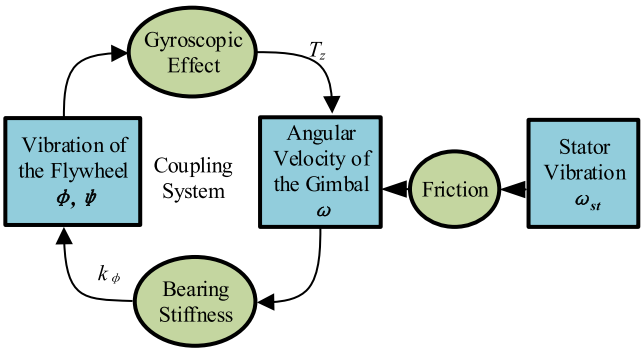

FIGURE 9. The mechanism of the coupling system.

IV. SIMULATIONS AND DISCUSSIONS

In order to further understand the coupling mechanism in the dynamic system of the presented SGCMG, numerical simulations are carried out. These simulations are based on the commercial software MATLAB/Simulink. The Runge-Kutta method is used for the numerical simulations of the model. The mechanical parameters of the SGCMG are shown

TABLE 1. Mechanical parameters of the SGCMG.

Structure	Parameters	Notation	Value
Flywheel	Radial moments of the inertia	I_r	2.9e-3 kg·m^2
	Polar moments of the inertia	I_p	5.46e-3 kg·m^2
	Dynamic unbalance weight	U_d	2e-6 kg·m^2
Gimbal	Distance between bearings	l	0.1 m
	Moment of inertia	I_{gy}	0.27e-3 kg·m^2
	Damping	C_R	2.46e-4 kg·m^2/s
Bearing	Diameter of the roller	d	2e-3 m
	Nominal diameter	D_m	9.5e-3 m
	Initial contact angle	α	10°
	Number of the roller	Z	8
	Inner raceway curvature radius coefficient	f_i	0.515
	Outer raceway curvature radius coefficient	f_o	0.525
	Elastic modulus of the roller	E_r	320e9 pa
	Elastic modulus of the raceway	E_R	210e9 pa
	Possion's ratio of the roller	v_r	0.26
	Possion's ratio of the raceway	v_R	0.3
USM	Rotor's polar moments of the inertia	I_R	3.5e-6 kg·m^2
	Eigen frequency of the stator	f_n	4.0e4 Hz
	Mechanical coefficient	c	1.74e-9
	Damping of the stator	ς	0.01
	Mean radius of the rotor contact area	r_0	35e-3 m
	Stribeck velocity	ω_s	2.6 rad/s
	Stribeck friction	F_S	16.6 N
	Coulomb friction	F_C	10 N

in Table 1. The time step is 1e^{-4} s in numerical simulations. Some of the parameters, which describing the friction process, are difficult to be measured directly, so the system identification method is used to get the relative parameters [36].

The stiffness k_Φ in the vibration Eq. (22) is an important parameter, which can be influenced not only by the physical parameters of the bearing but also by the working condition of the flywheel. In this section, the influence of the rotation speed, the nominal diameter and the number of the roller on the stiffness are analyzed.

As shown in Fig. 10, the k_Φ will increases along with the speed increase of the flywheel and the gimbal. Due to the gyroscopic effect in the SGCMG, according to Eq. (10) the radial load F_r is influenced greatly by the speeds of the gimbal and the flywheel. With the speed increasing, the radial load applied on the bearing increases, which is a dynamic force and cause the stiffness increases.

The influences of the physical parameters of the bearing, the nominal diameter and the number of the roller, are shown in Fig. 11. During the simulation, the velocity of the gimbal is kept at a constant value of 120 °/s. The influences of the nominal diameter are shown in Fig. 11(a), and the k_Φ increases along with the increase of the nominal diameter at different flywheel speed. With the nominal diameter increases, the bearing coefficient γ decreases, which cause the contact ellipse increases and the normal contact stress decreases. The influences of the number of the roller are shown in Fig. 11(b), which indicates that he k_Φ increases along with the increase of the number of the roller at different flywheel speed. That is the number of the roller directly influence the largest contact

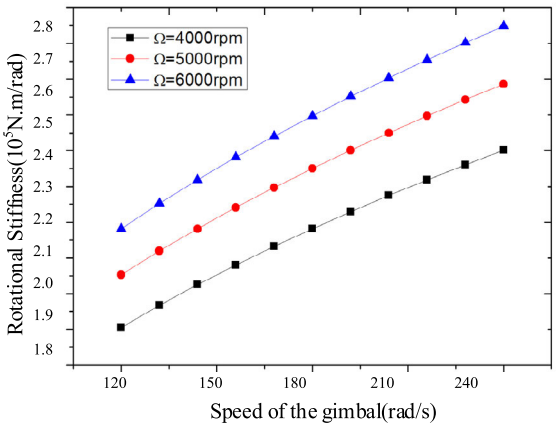

FIGURE 10. The influence of the rotate speed.

stress of the roller of the bearing. With the increases of the roller number, the largest contact stress decreases and the contact deformation of the bearing decreases, which lead to the increases of the bearing's stiffness. These dimension parameters influence the contact in the bearing.

The vibration of the flywheel due to the dynamic unbalanced mass would affect the rotation of the gimbal and the output torque. Conversely, the flywheel is also influenced by the gimbal's running. The vibration analyses of the flywheel include mainly the eigen frequency and the amplitude. To analyze the influence of the coupling system, the stiffness in the normal model is seen as a constant of 1.9e^5 Nm/rad and the rotation speed of the gimbal is kept at a constant of 120°/s during the simulations.

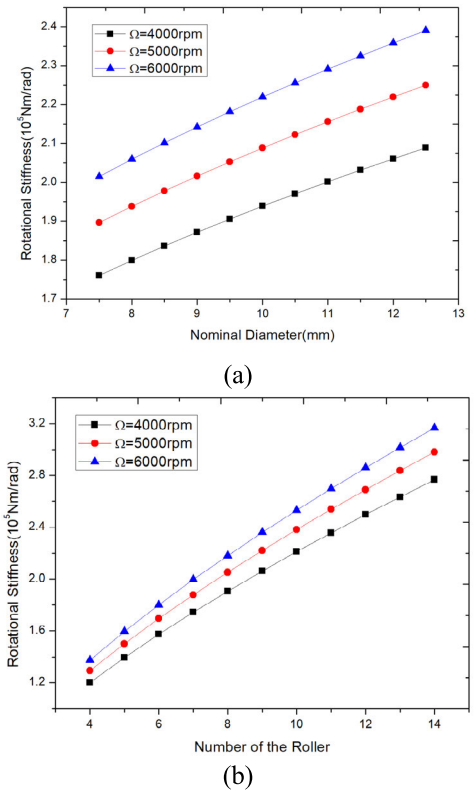

FIGURE 11. The influences of the physical parameters: (a) The nominal diameter (b) The number of the roller.

The eigen frequency of the system is affected by the rotation speed, and the relationship between the eigen frequency and the rotation speed can be presented by the Campbell diagram as shown in Fig. 12. From Eq. (25) in section 3.1, the eigen frequency of the system is associated with the speed of the flywheel. The eigen frequency of the backward precession decreases and the eigen frequency of the forward precession increases with the speed increases of the flywheel. However, the eigen frequency of back precession mode increases considering the coupling effect. The eigen frequency of the coupled system is lower than the frequency of the uncoupled system, especially in the low speed range.

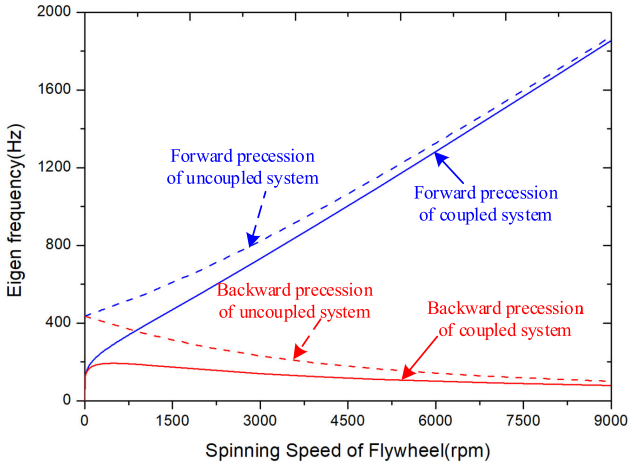

FIGURE 12. The Campbell diagram.

The gimbal is directly driven by the ultrasonic motor and affected by the gyroscopic torque T_z. A dynamic simulation of the flywheel-bearing system is conducted while the speed of the flywheel is kept at 4500 r/min. The gimbal driven by the USM at open-loop state, and the working conditions of the USM are shown in Table 2.

TABLE 2. Working parameters of the USM.

Parameters	Notation	Value
frequency	f	45kHz
Voltage	V_0	400V(Peak to peak)
Phase difference	α	pi/2

The stiffness of the bearing is time-varying, and the fluctuation of the stiffness is periodically as shown in Fig. 13. The fluctuation of the stiffness is divided into two periods: the unstable period and the stable period. In the unstable period, the stiffness's amplitude attenuates rapidly. This phenomenon is caused by the high frequency components, which is caused by the instability of the gimbal speed and the transient solution of the flywheel-bearing system. The high frequency component decays over the unstable period, and then it reaches the stable region. In the stable region, the fluctuating amplitude of the stiffness is relative to the speed of the flywheel.

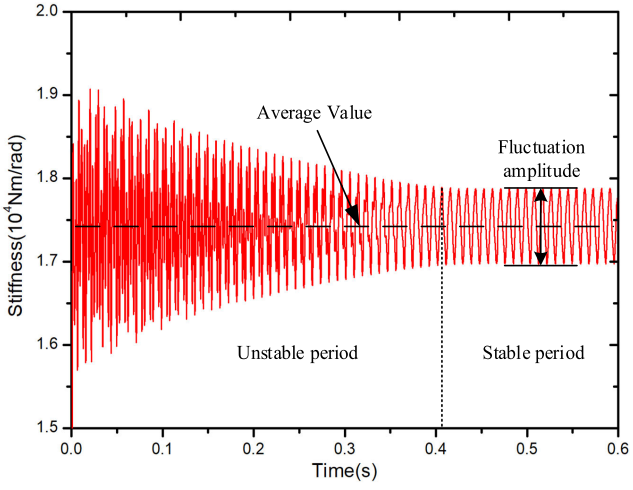

FIGURE 13. The stiffness variation.

The relation between the speed of the flywheel and the stiffness are shown in Fig. 14. The black line is the fluctuation amplitude of the stiffness at different flywheel speed and the red line is the average value of the stiffness. The value of those two parameters increase with the speed increasing of the flywheel. The fluctuation amplitude value grows faster than the average value, because the fluctuation amplitude is mainly determined by the speed fluctuation of the gimbal.

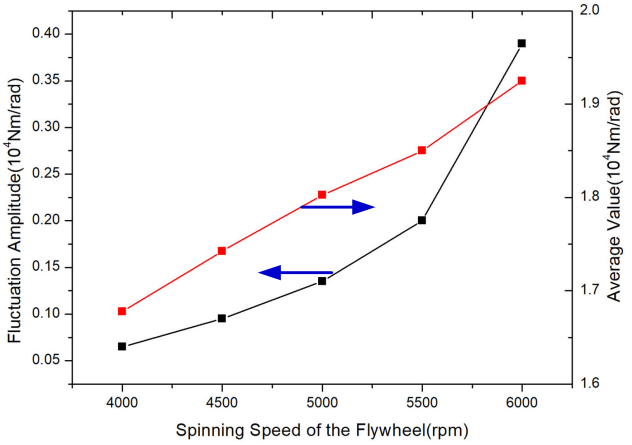

FIGURE 14. The relation between of the flywheel's speed and the stiffness.

The disturbance torque T_z in Eq. (9) applied on the gimbal increases with the speed increasing of the flywheel, which cause the fluctuation amplitude of the gimbal speed increases. The increasing of the gimbal speed fluctuation results in the increasing of the stiffness fluctuation. The increasing of the average value is mainly caused by the increasing of the flywheel speed.

The vibration of the flywheel-bearing system calculated by the coupled model and the normal model are shown in Fig.15. The stiffness of the normal model is $1.75e^4$ Nm/rad. Considering the coupling effect, the unstable period is 0.41s as shown in Fig.15(a), which is longer than 0.31s shown in Fig.15(b) of the normal model where the coupling effect is ignored. The transient process is mainly due to the instability of the stiffness considering the coupling, and at the stable period the amplitude is mainly affected by the speed of the flywheel.

The simulating results of the gimbal speed at 8 °/s for the coupled model and the normal model are shown in Fig. 16, where the flywheel speed is 4000 r/min. Fig. 16(a) is the simulation results of the coupled model, and Fig. 16(b) is the simulation results ignoring the coupling effect in the system. As shown in the zoomed part, the coupled model has shown high-frequency components compared with the normal model. This could be analyzed by the Fast Fourier Transform (FFT), and the results of FFT are shown in Fig. 17.

From the FFT results shown in Fig. 17, the third component of the gimbal's speed increases with the speed increases of the flywheel. When the flywheel's speed reaches 6000 r/min, the frequency of the exciting torque is 100 Hz. And in fig.12, the eigen frequency of the back precession is near 100 Hz, when the flywheel rotates at the speed of 6000 r/min. With the exciting of the rotating flywheel, the amplitude of the third order component is approximately equal to the first order component. The increased high order component will affect the stability of the gimbal speed and reacts on the fluctuation of the stiffness of the bearing.

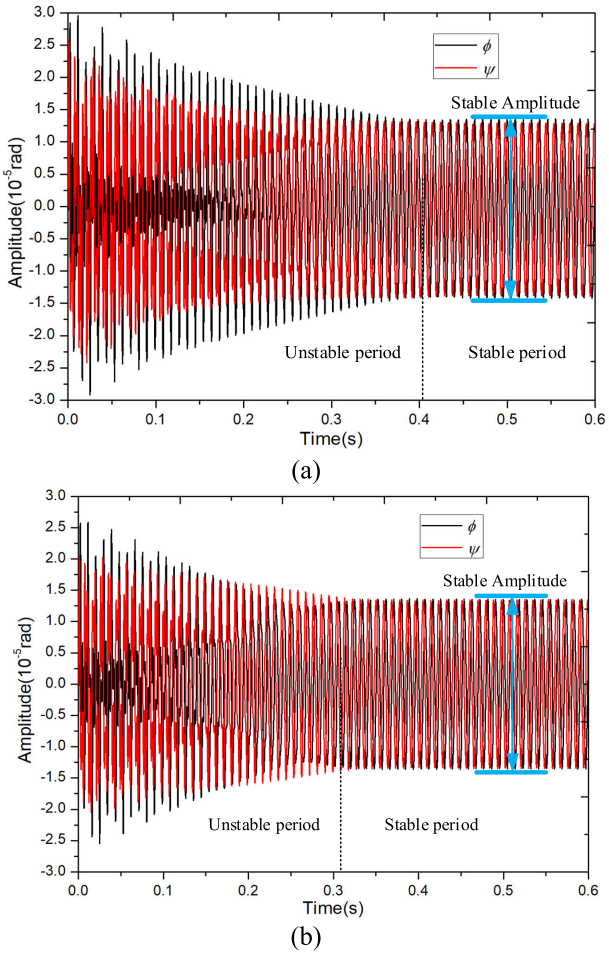

FIGURE 15. The vibration of the flywheel-bearing system: (a) Coupled model (b) Normal model.

V. EXPERIMENTS AND DISCUSSIONS

To verify the numerical simulations, an experimental platform was established as shown in Fig. 18. It consists of the SGCMG prototype, a Digital Signal Processor (DSP, TMS320F28335, TI, U.S.) and a data acquisition board (PCI-1716, Advantech Co., Ltd, Taiwan, China). The SGCMG prototype consists of the encoder (DS-70-64-3SH, Netzer Precision Motion Sensors Ltd, Israel) and the USM (PMR-70ZK, NUAA Super Control Technologies Co., Ltd, Jiangsu, China). The SGCMG prototype was assembled on the base. The angular position and the rotation speed of the gimbal are measured through the encoder, the speed of the flywheel is measured by the hall sensor attached on the stator of the high-speed motor. The experimental data are acquired and processed by the DSP. The processed data are transmitted to the PC via the PCI-1716. The functional diagram of the experimental system is shown in Fig. 19. The sample period of the testing system is 0.001s.

Fig.20 shows the measured gimbal speed when the gimbal motor is not working, while the flywheel speed is 4000 r/min. It can be seen from the experimental results that there is dynamic velocity around the gimbal axis, which could be

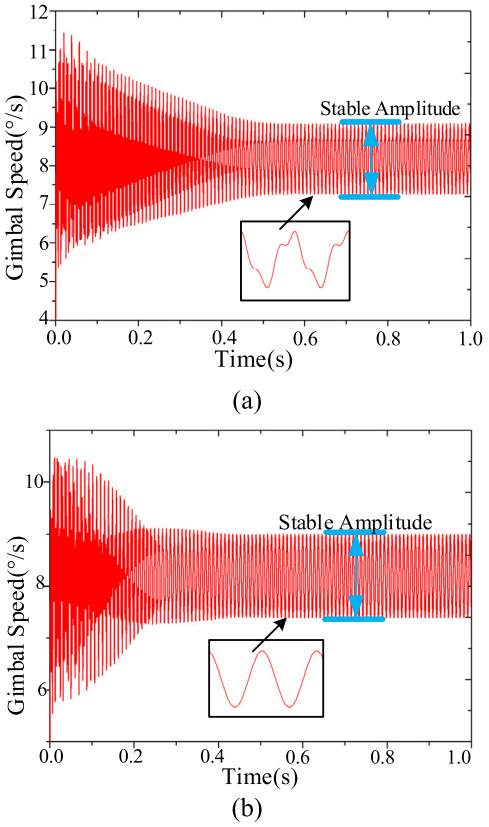

FIGURE 16. The gimbal speed: (a) The coupled model (b) The normal model.

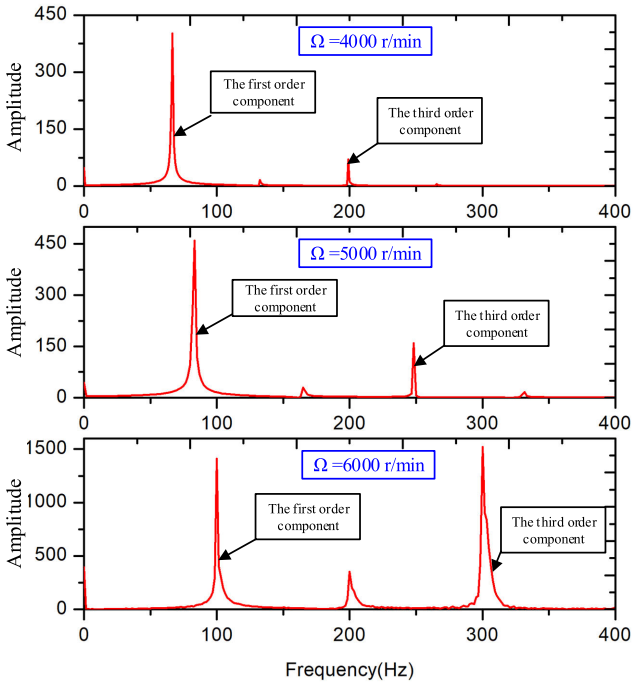

FIGURE 17. The FFT results of the gimbal speed at different flywheel speed.

explained by the disturbance torque T_z in Eq. (9). In this situation, the gyroscopic coupling effect is very small since the

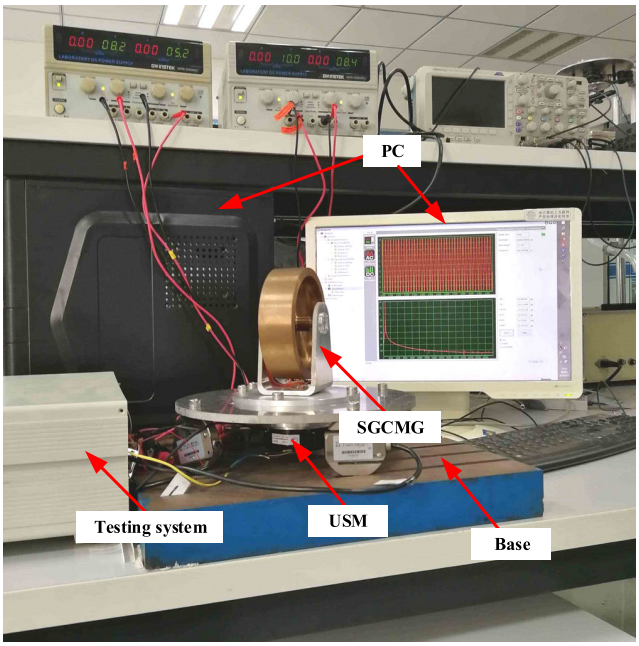

FIGURE 18. The experimental system.

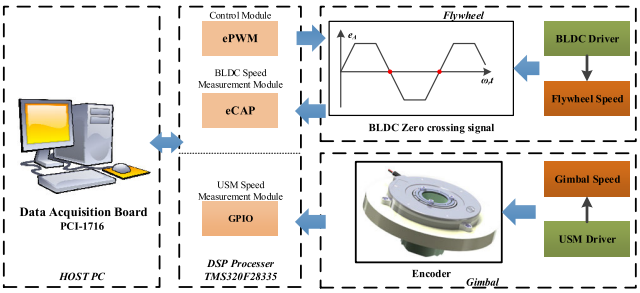

FIGURE 19. The functional diagram of the experimental system.

amplitude of the gimbal speed is very small. The simulation results with the constant stiffness of 2.2e4 Nm/rad is shown in Fig. 20(a), the speed of the gimbal varies from −0.045°/s to 0.045°/, which matches well with the experiment results in Fig. 20(b).

The disturbance torque caused by the coupling effect has great impact on the rotation of the gimbal. The gimbal speed measured by the encoder and comparison are shown in Fig. 21. It can be seen from Fig. 21(a) that the gimbal speed at different flywheel speed are affected by the flywheel speed. The gimbal speed fluctuation amplitude is 1.5°/s, 2.2°/s and 4.65°/s, and the standard deviation of the gimbal speed is 0.41, 0.57 and 1.17 when the flywheel speed is 4000 r/min, 5000 r/min and 6000 r/min, respectively. Fig. 21(b) is the comparison with the simulation results of the coupled model and the normal model. As shown in Fig. 21(b), with the speed increases of the flywheel the stable amplitude of the gimbal speed fluctuation increasing. When the speed of the flywheel is 4000 r/min, the fluctuation amplitudes are similar for the normal model and the coupled model. But when the flywheel speed increases, due to the fast increases

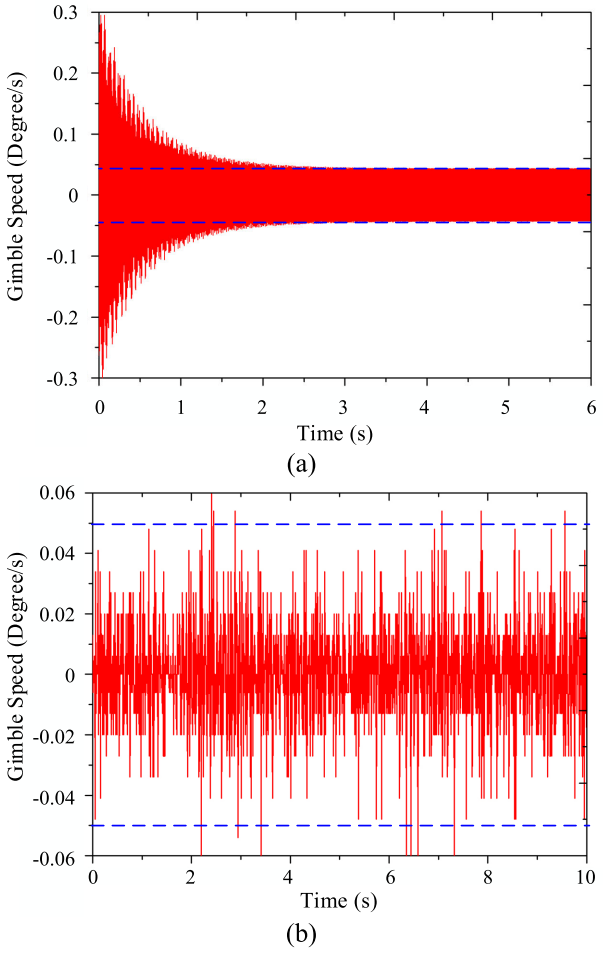

FIGURE 20. The gimbal speed when the gimbal motor is not working: (a) Simulation, (b) Experiments.

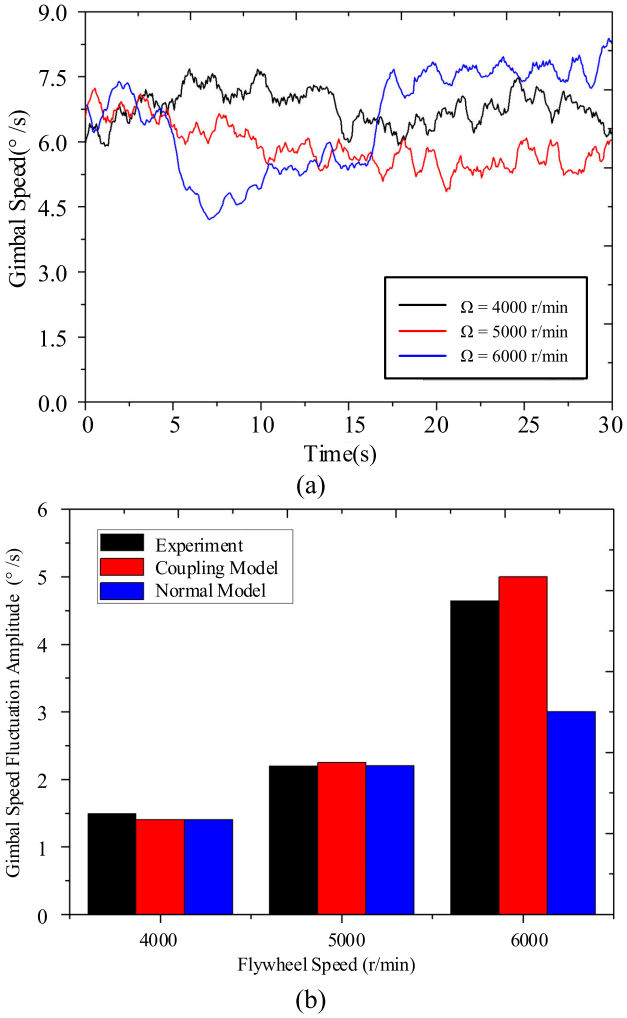

FIGURE 21. The gimbal running is affected by the flywheel speed: (a) The experiment with the gimbal speed of 6°/s, (b) The comparison with the simulation results.

of the 3rd component in Fig. 17, the fluctuation amplitude of the coupled model increases faster than the normal model. The experimental results also verify the coupled model. That is the coupling effect is enhanced with the speed increasing of the flywheel.

The dynamic performance of the gimbal is significant in the SGCMG system. To learn about how the dynamic performance of the gimbal affected by the flywheel speed, speed step experiments are carried out as shown in Fig. 22. The experimental results are compared with the simulations. The experimental results show that the gimbal speed fluctuation increases with the gimbal speed increasing. When the speed step is applied on the gimbal speed, the speed increases first and then decreases to a stable value. The settling time of the gimbal speed are 12.5s, 17.5s and 22.5s corresponding to the flywheel speed of 4000 r/min, 5000 r/min and 6000 r/min, respectively. The setting time increase approximately linear with the increase of the flywheel speed, which means that the influence of the gimbal speed on the coupling effect is smaller than that of the flywheel speed.

The FFT results of the gimbal speed around 8 °/s obtained from the experiments are shown in Fig. 23. As shown in the figure, there are exists the disturbance components of the 1^{st}, 2^{nd} and 3^{rd} of the flywheel rotational frequency in the spectrum. Theoretically, the higher the flywheel speed is, the stronger the coupling effect becomes. But the 1^{st} order component values have shown a decreasing trend as the flywheel speed increase. This is that the CMG connects with the base through three force sensors, which have a certain degree of flexibility. The flexible support acts as a lowpass filter for the gimbal speed. The 3^{rd} order component has the amplitude of 0.12 with the flywheel speed of 5000rpm while the amplitude of 0.16 with the flywheel speed of 6000rpm verified the theory analysis. However, the amplitude of 4000rpm is 0.3, which is much higher than the amplitude of 5000rpm and 6000rpm. Due to the flexible support used to install the CMG, the whole system has a resonant frequency near 66Hz (4000rpm), which cause the data exception of the 4000rpm.

From the experimental results, the coupling effect in the SGCMG affects the rotation of the gimbal greatly. The stability of the gimbal affects the performance of SGCMG greatly, which is important for the high precision pointing

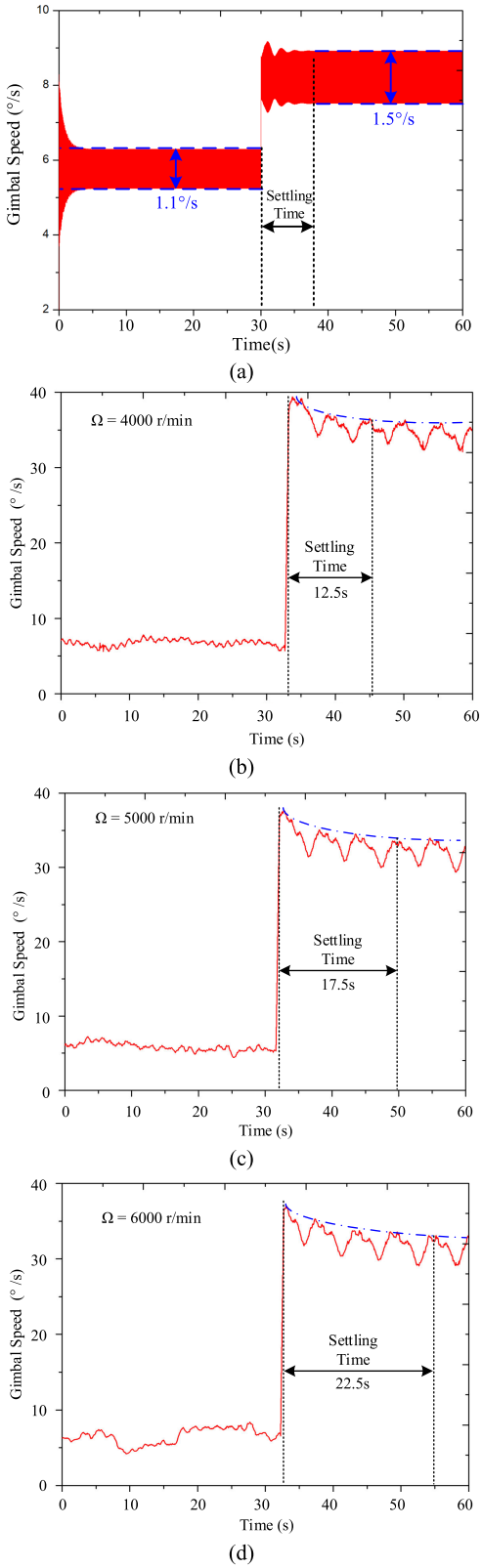

FIGURE 22. The gimbal speed step: (a) Simulation result (b) Experiment result with the flywheel speed of 4000 r/min (c) Experiment result with the flywheel speed of 5000 r/min (d) Experiment result with the flywheel speed of 6000 r/min.

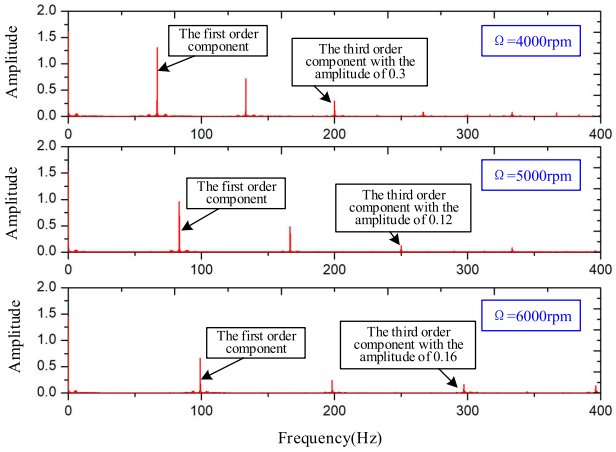

FIGURE 23. The FFT results of the experimental gimbal speed at different flywheel speed.

performance of the satellites. Based on the coupled model in this research, the more accurate predictions in the control system are available. The flexible support has great impact on the gimbal control system. This is our future research interest.

VI. CONCLUSION

In this research, we focused on the coupling relationship between the flywheel vibration and the gimbal rotation through the variable stiffness of the bearing. Using the Hertz contact theory, the mathematical model of the supporting bearings is established, and the stiffness of the bearings is affected by the load that applied on the bearing. Based on the bearing model, the vibration equation with variable stiffness of the flywheel-bearing system is developed. Considering the effect of the gyroscopic torque, the stiffness of the bearing is affected by the speed of the gimbal and the flywheel, resulting in the influence on the flywheel vibration characteristic. In addition, the rotation of the gimbal is affected by the gyroscopic torque generated by the flywheel micro-vibration as well. The coupling influence among the bearing stiffness, the flywheel vibration and the gimbal rotation are analyzed by the simulations and experiments. Through the numerical simulations and the experiments, the coupling system has the following characteristics:

a). The eigen frequency of the forward precession and the backward precession have close relation with the speed of the flywheel.

b). The vibrating amplitude of the flywheel and the speed fluctuation of the gimbal increases when considering the coupling effect in the system.

c). The coupling effect is enhanced when the spinning speed of the flywheel increases. The high order component of the gimbal speed increases fast when the flywheel speed increases.

This coupling model proposed in this research could guide the design of the anti-disturbance control algorithm for the gimbal servo system. However, there're still many factors that influence the working of the SGCMG such as the elasticity of the frame, the nonlinear characteristic of the USM and the temperature. That would be our future research plan.

REFERENCES

[1] R. Masterson, D. Miller, and R. Grogan, "Development of empirical and analytical reaction wheel disturbance models," in *Proc. 40th Struct., Structural Dyn., Mater. Conf. Exhib.*, Apr. 1999, pp. 1–12.
[2] B. J. Kawak, "Development of a low-cost, low micro-vibration CMG for small agile satellite applications," *Acta Astronautica*, vol. 131, pp. 113–122, Feb. 2017.
[3] Y. Zhu, Y. Gao, C. Xu, J. Zhao, H. Jin, and J. Lee, "Adaptive control of a gyroscopically stabilized pendulum and its application to a single-wheel pendulum robot," *IEEE/ASME Trans. Mechatronics*, vol. 20, no. 5, pp. 2095–2106, Oct. 2015.
[4] B. Thornton, T. Ura, Y. Nose, and S. Turnock, "Zero-G class underwater robots: Unrestricted attitude control using control moment gyros," *IEEE J. Ocean. Eng.*, vol. 32, no. 3, pp. 565–583, Jul. 2007.
[5] S. Basaran, S. Sivrioglu, and E. Zergeroglu, "Composite adaptive control of single gimbal control moment gyroscope supported by active magnetic bearings," *J. Aerosp. Eng.*, vol. 30, no. 1, Jan. 2017, Art. no. 04016074.
[6] N. C. Townsend and R. A. Shenoi, "Gyrostabilizer vehicular technology," *Appl. Mech. Rev.*, vol. 64, no. 1, pp. 1–14, Jan. 2011.
[7] F. A. Leve, "Evaluation of steering algorithm optimality for single-gimbal control moment gyroscopes," *IEEE Trans. Control Syst. Technol.*, vol. 22, no. 3, pp. 1130–1134, May 2014.
[8] J. Fang and Y. Ren, "High-precision control for a single-gimbal magnetically suspended control moment gyro based on inverse system method," *IEEE Trans. Ind. Electron.*, vol. 58, no. 9, pp. 4331–4342, Sep. 2011.
[9] M. Lu, Y. Wang, Y. Hu, L. Liu, and N. Su, "Composite controller design for PMSM direct drive SGCMG gimbal servo system," in *Proc. IEEE Int. Conf. Adv. Intell. Mechatronics (AIM)*, Jul. 2017, pp. 106–112.
[10] C. S. Zhao, *Ultrasonic Motors Technologies and Applications*. Springer, 2011.
[11] [Online]. Available: http://jsnews2.jschina.com.cn/system/2013/12/18/019667921.shtml
[12] Y. Bar-Cohen, X. Bao, and H. Das, "Ultrasonic motors (USM)—An emerging actuation technology for planetary applications," *J. Acoust. Soc. Amer.*, vol. 108, no. 5, p. 2494, Nov. 2000.
[13] U. Roberto and M. Flavia, "Artemis micro-vibration environment prediction, spacecraft structures, materials and mechanical testing," in *Proc. Eur. Conf. Germany*, 1998, pp. 4–6.
[14] T. Shimizu, S. Nagata, S. Tsuneta, T. Tarbell, C. Edwards, R. Shine, C. Hoffmann, E. Thomas, S. Sour, R. Rehse, O. Ito, Y. Kashiwagi, M. Tabata, K. Kodeki, M. Nagase, K. Matsuzaki, K. Kobayashi, K. Ichimoto, and Y. Suematsu, "Image stabilization system for Hinode (Solar-B) solar," *Opt. Telescope Solar Phys.*, vol. 249, pp. 221–232, Apr. 2008.
[15] C. L. Foster, M. L. Tinker, G. S. Nurre, and W. A. Till, "Solar-array-induced disturbance of the hubble space telescope pointing system," *J. Spacecraft Rockets*, vol. 32, no. 4, pp. 634–644, Jul. 1995.
[16] C. G. Majumder, M. S. Siva, K. A. Kumar, and N. K. Philip, "Control algorithms for improved high pointing accuracy and rate stability in agile imaging spacecrafts," in *Proc. Indian Control Conf. (ICC)*, Jan. 2017, pp. 93–98.
[17] D. Addari, G. S. Aglietti, and M. Remedia, "Experimental and numerical investigation of coupled microvibration dynamics for satellite reaction wheels," *J. Sound Vib.*, vol. 386, pp. 225–241, Jan. 2017.
[18] Q. Luo, D. Li, and J. Jiang, "Analysis and optimization of microvibration isolation for multiple flywheel systems of spacecraft," *AIAA J.*, vol. 54, no. 5, pp. 1719–1731, May 2016.
[19] C. E. Eyerman, "System engineering approach to disturbance minimization for spacecraft utilizing controlled structures technology," M.S. thesis, Aeronautics and Astronautics, Reston, VA, USA, 1990.
[20] W. Zhou, D. Li, Q. Luo, and K. Liu, "Analysis and testing of microvibrations produced by momentum wheel assemblies," *Chin. J. Aeronaut.*, vol. 25, no. 4, pp. 640–649, Aug. 2012.
[21] W.-Y. Zhou, G. S. Aglietti, and Z. Zhang, "Modelling and testing of a soft suspension design for a reaction/momentum wheel assembly," *J. Sound Vib.*, vol. 330, nos. 18–19, pp. 4596–4610, Aug. 2011.
[22] Q. Luo, D. Li, W. Zhou, J. Jiang, G. Yang, and X. Wei, "Dynamic modelling and observation of micro-vibrations generated by a single gimbal control moment gyro," *J. Sound Vib.*, vol. 332, no. 19, pp. 4496–4516, Sep. 2013.
[23] G. Jang and S.-W. Jeong, "Vibration analysis of a rotating system due to the effect of ball bearing waviness," *J. Sound Vib.*, vol. 269, nos. 3–5, pp. 709–726, Jan. 2004.
[24] H. Cao, "Time varying bearing stiffness and vibration response analysis of high speed rolling bearing-rotor systems," *J. Mech. Eng.*, vol. 50, no. 15, p. 73, 2014.
[25] A. Muszynska, "Forward and backward precession of a vertical anisotropically supported rotor," *J. Sound Vib.*, vol. 192, no. 1, pp. 207–222, Apr. 1996.
[26] Q. Luo, D. Li, and J. Jiang, "Coupled dynamic analysis of a single gimbal control moment gyro cluster integrated with an isolation system," *J. Sound Vib.*, vol. 333, no. 2, pp. 345–363, Jan. 2014.
[27] N. S. Chana, Z. F. Reif, and R. G. S. Gaspar, "Preliminary study of rolling element bearing behavior under radial loading," in *Proc. 17th Int. Modal Anal. Conf.*, 1999, pp. 1968–1973.
[28] J. W. Luo and T. Y. Luo, *Analysis Calculation and Application of Rolling Bearing*. Beijing, China: Machine, 2009.
[29] Y. Zhang and J. Zhang, "Disturbance characteristics analysis of CMG due to imbalances and installation errors," *IEEE Trans. Aerosp. Electron. Syst.*, vol. 50, no. 2, pp. 1017–1026, Apr. 2014.
[30] L. Huang, Z. Wu, and K. Wang, "Indirect measurement of rotor dynamic imbalance for control moment gyroscopes via gimbal disturbance observer," *Sensors*, vol. 18, no. 6, p. 1873, Jun. 2018.
[31] H. Wang, Q. Han, and D. Zhou, "Output torque modeling of control moment gyros considering rolling element bearing induced disturbances," *Mech. Syst. Signal Process.*, vol. 115, pp. 188–212, Jan. 2019.
[32] C. Canudas-de-Wit, "Control design for ultrasonic motors with dynamic friction interface," *IFAC Proc. Volumes*, vol. 32, no. 2, pp. 970–974, Jul. 1999.
[33] J. Sopanen and A. Mikkola, "Dynamic model of a deep-groove ball bearing including localized and distributed defects. Part 2: Implementation and results," *Proc. Inst. Mech. Eng. K, J. Multi-Body Dyn.*, vol. 217, no. 3, pp. 213–223, Sep. 2003.
[34] T. Harris and M. Kotzalas, *Rolling Bearing Analysis*. Boca Raton, MA, USA: Taylor & Francis, 2007.
[35] M. Kuhne, R. G. Rochin, R. S. Cos, G. J. R. Astorga, and A. Peer, "Modeling and two-input sliding mode control of rotary traveling wave ultrasonic motors," *IEEE Trans. Ind. Electron.*, vol. 65, no. 9, pp. 7149–7159, Sep. 2018.
[36] R. Garcia-Rochin, M. Kuhne, R. Santiesteban-Cos, G. J. Rubio-Astorga, and A. Peer, "Second-order model for rotary traveling wave ultrasonic motors," in *Proc. IEEE-RAS 15th Int. Conf. Hum. Robot.*, Nov. 2015, pp. 991–996.

SONG PAN (Member, IEEE) was born in 1978. He received the B.S. degree from the Shandong University of Technology, Zibo, China, and the M.S. and Ph.D. degrees from the Nanjing University of Aeronautics and Astronautics (NUAA), Nanjing, China, in 2005, and 2009, respectively.

He was a Postdoctoral Researcher of the motor and electrical engineering with NUAA, from 2009 to 2010, where he is currently a Lecturer with the College of Aerospace Engineering. He is the author of more than 20 articles and more than ten inventions. His research interests include drive and control technology of piezoelectric actuator and ultrasonic motor.

Dr. Pan is a member of the Chinese Association of Automation and the Chinese Society of Aeronautics and Astronautics.

FAN ZHANG XU was born in 1995. He received the B.S. degree from the Nanjing University of Aeronautics and Astronautics (NUAA), Nanjing, China, in 2016, where he is currently pursuing the Ph.D. degree.

His research interest includes structure of piezoelectric actuator and its application in astronautic mechanics.

LEI CHEN was born in 1994. He received the B.S. degree in aircraft design and engineering and the M.S. degree in mechanical design and theory from the Nanjing University of Aeronautics and Astronautics (NUAA), Nanjing, Jiangsu, in 2016 and 2019, respectively, where he is currently pursuing the Ph.D. degree in measurement and testing technology and instruments.

His research interests include piezoelectric actuating, ultrasonic driving, and electromagnetic motors.

WEIQING HUANG was born in Nantong, China, in 1965. He received the B.S. and M.S. degrees from NUAA, in 1987 and 1990, respectively, and the Ph.D. degree from The Hong Kong University of Science and Technology, Hong Kong, in 1999. He is currently a Professor with the School of Mechanical and Electric Engineering, Guangzhou University. His current research interests include motor design and control based on piezoelectric actuator.

JINTAO WU is currently an Associate Professor with the Beijing Institute of Control Engineering. His research interests include spacecraft attitude determination and attitude control actuators.